# Dynamics and Predictability of Downward-Propagating Stratospheric Planetary Waves Observed in March 2007



Mukougawa, Hitoshi; Noguchi, Shunsuke; Kuroda, Yuhji; Mizuta, Ryo; Kodera, Kunihiko

# Dynamics and Predictability of Downward-Propagating Stratospheric Planetary Waves Observed in March 2007

HITOSHI MUKOUGAWA

*Disaster Prevention Research Institute, Kyoto University, Uji, Japan*

SHUNSUKE NOGUCHI, YUHJI KURODA, AND RYO MIZUTA

*Meteorological Research Institute, Tsukuba, Japan*

KUNIHIKO KODERA

*Solar-Terrestrial Environment Laboratory, Nagoya University, Nagoya, Japan*

(Manuscript received 17 November 2016, in final form 14 June 2017)

ABSTRACT

The predictability of a downward-propagating event of stratospheric planetary waves observed in early March 2007 is examined by conducting ensemble forecasts using an AGCM. It is determined that the predictable period of this event is about 7 days. Regression analysis using all members of an ensemble forecast also reveals that the downward propagation is significantly related to an amplifying quasi-stationary planetary-scale anomaly with barotropic structure in polar regions of the upper stratosphere. Moreover, the anomaly is 90° out of phase with the ensemble-mean field. Hence, the upper-stratospheric anomaly determines the subsequent vertical-propagating direction of incoming planetary waves from the troposphere by changing their vertical phase tilt, which depends on its polarity. Furthermore, the regressed anomaly is found to have similar horizontal structure to the pattern of greatest spread among members of the predicted upper-stratospheric height field, and the spread growth rate reaches a maximum prior to the occurrence of the downward propagation. Hence, the authors propose a working hypothesis that the regressed anomaly emerges as a result of the barotropic instability inherent to the upper-stratospheric circulation.

In fact, the stability analysis for basic states constituting the ensemble-mean forecasted upper-stratospheric streamfunction field using a nondivergent barotropic vorticity equation on a sphere supports this hypothesis. Thus, the barotropic instability inherent to the distorted polar vortex in the upper stratosphere forced by incoming planetary waves from the troposphere determines whether the planetary waves are eventually absorbed or emitted downward in the stratosphere.

## 1. Introduction

Recently, Kodera et al. (2008) revealed observational evidence of downward-propagating planetary waves from the stratosphere into the troposphere just after a stratospheric sudden warming (SSW) event in early March 2007. Based on a detailed analysis of the three-dimensional propagation of the planetary-scale wave packet, they showed that the wave packet incoming from the troposphere over Eurasia gradually deflects eastward and then propagates downward into the troposphere over the American–Atlantic sector. Based on several case studies, Kodera et al. (2013) also elucidated that the downward-propagating planetary wave packet promotes the formation of tropospheric blocking over the Pacific sector as well as a trough over eastern Canada. Thus, the downward-propagating stratospheric planetary wave exerts a significant zonally asymmetric influence on the tropospheric circulation. This contrasts with the zonally symmetric influence of a downward-migrating annular-mode anomaly indicated by Baldwin and Dunkerton (1999, 2001).

Although there is robust observational evidence of the downward propagation of stratospheric planetary waves, its occurrence mechanism and the related dynamics still remain controversial. By conducting a zonal wavenumber decomposition analysis on observed

*Corresponding author*: Hitoshi Mukougawa, mukou@dpac.dpri.kyoto-u.ac.jp

DOI: 10.1175/JAS-D-16-0330.1

downward-propagating planetary waves in the stratosphere, Perlwitz and Harnik (2003) argued that the existence of a reflecting surface for vertical propagation at around 5 hPa is key to inducing the downward propagation. On the other hand, Tomikawa (2010) suggested that the overreflection of the zonal wavenumber (WN)-1 component at the critical surface is important in producing downward-propagating planetary waves.

However, since these arguments are based on the quasi-linear framework of wave and zonal-mean flow interaction, the applicability to downward-propagating events frequently observed just after SSWs with a highly distorted polar vortex is still uncertain. In fact, a limitation of the quasi-linear framework based on the zonally symmetric basic state was suggested by Noguchi et al. (2016), which assessed the predictability of an SSW event in January 2009 with vortex splitting. By conducting a series of ensemble reforecasts using an AGCM, they showed that predicted planetary waves are absorbed in the stratosphere for a group of ensemble members in predicting the vortex splitting, whereas they propagate downward for another group. However, the zonal-mean basic states of both groups in the upper stratosphere satisfy a preferable condition for the wave reflection. Hence, they insisted that zonal asymmetry of the basic state would be more relevant to the different propagating properties of the planetary wave during this event.

The predictability of the downward-propagation event of the planetary wave must also be revealed by taking account of its critical influence on surface weather (Kodera et al. 2008, 2013). So far, no attempts have been made to assess the practical predictability of the downward propagation of the planetary wave using sophisticated AGCMs. Hence, in this study, we have conducted a series of ensemble reforecast AGCM experiments using the same experimental setting of Noguchi et al. (2016) for the downward-propagation event of planetary waves in March 2007, for which the observed time evolution was revealed by Kodera et al. (2008). It is noteworthy that the downward propagation becomes most prominent on 5 March just after a displacement-type SSW event in which the North Pole temperature had attained local maxima on 24 February and 4 March (Kodera et al. 2008, 2013).

Analyses on all ensemble members also help us to speculate as to the occurrence mechanism of the targeted atmospheric event. In fact, atmospheric anomalies during some SSW events have been clarified in some studies using ensemble forecasts. Mukougawa et al. (2005) pointed out the importance of the persistence of tropospheric blocking over the Atlantic in the occurrence of a vortex-displacement-type SSW in December 2001, which has been also confirmed by a complementary numerical experiment using an AGCM (Mukougawa et al. 2007). Noguchi et al. (2016) detected the important role of a preexisting stratospheric circulation anomaly in the occurrence of vortex splitting during the SSW event in January 2009. Here, through analysis on an ensemble reforecast experiment, we aim to build a plausible hypothesis for the emergence mechanism of downward-propagating planetary waves in the stratosphere in March 2007.

Constructing a robust dynamical framework with which to understand the predictability change during the downward-propagating event in March 2007 is another important challenge to be addressed in this paper. To accomplish this formidable task, we must first confirm the correspondence between the practical and intrinsic predictability. Although the practical predictability of the real atmosphere is easily assessed by the ensemble-mean forecast error or spread of ensemble forecasts with many members, we cannot necessarily guarantee that the obtained practical predictability corresponds to the intrinsic predictability, which represents the instability of the atmospheric state trajectory in phase space. The intrinsic predictability is quantified by a local divergent rate of nearby trajectories in phase space based on a tangent linear equation describing the evolution of the infinitesimally perturbed trajectory in the vicinity of the basic trajectory, such as the Lorenz index (e.g., Mukougawa et al. 1991), which is given by singular values of the error matrix (Lorenz 1965) and the local Lyapunov exponent (e.g., Nese 1989). The Lyapunov exponents represent global characteristics of the intrinsic predictability averaged over the flow attractor. However, since the real atmospheric state trajectory is embedded in infinite-dimensional phase space, it is practically impossible to compute these indices for the real atmosphere. Therefore, we have to compromise by using simplified models with a rather coarse horizontal resolution representing a limited class of atmospheric motions to estimate the intrinsic predictability. For example, in the pioneering work of Kimoto et al. (1992), which revealed the predictability change during a tropospheric blocking event, they used a truncated barotropic model to estimate intrinsic predictability. However, they recognized that the time evolution of the computed Lorenz index had only weak correspondence with that of the practical predictability assessed from operational forecasts. Hence, the dynamics relevant to the predictability change during the blocking event has not been clarified.

The weak correspondence between the practical and intrinsic predictability noted by Kimoto et al. (1992) is partially due to the fact that the barotropic model they

used to estimate the intrinsic predictability does not represent energetic baroclinic instability in the troposphere. However, the barotropic model would be suitable to examine the intrinsic predictability of stratospheric circulation. This expectation is plausible since many important dynamical aspects of the stratospheric circulation have been revealed using the barotropic model (e.g., Matsuno and Hirota 1966; Hirota 1967; Juckes and McIntyre 1987; Manney et al. 1991; Yoden and Ishioka 1993) owing to the predominance of planetary-scale dynamics and the absence of baroclinic instability in the stratosphere. Hence, we try to pursue the possibility that the practical predictability change of the stratospheric circulation during the downward-propagating event in March 2007 can be described by the time evolution of the intrinsic predictability of the stratospheric circulation assessed by a nondivergent barotropic vorticity equation. This attempt could be an invaluable milestone in revealing the dynamics of the predictability change of the stratospheric circulation during this event.

The remainder of this paper is organized as follows. Section 2 will describe the reanalysis dataset along with the experimental setup of the conducted ensemble reforecast experiment. In section 3, we will show results of the regression analysis as well as the EOF analysis using all ensemble members to elucidate the precursory signal for the downward propagation of the stratospheric planetary wave in March 2007. Based on this examination, we will postulate the following working hypothesis to explain the emergence of the precursor: the barotropic instability inherent to the distorted zonally asymmetric polar vortex in the upper stratosphere by incoming planetary waves from the troposphere determines whether the planetary waves are eventually absorbed or emitted downward in the stratosphere. In section 4, the dynamical stability of the distorted polar vortex will be examined by eigenvalue analysis of a nondivergent barotropic vorticity equation on a sphere, and we will demonstrate the relevance of the working hypothesis to the dynamics and predictability of downward-propagating planetary waves observed in March 2007. Section 5 will conclude the paper.

## 2. Data and experimental setup

### a. Data

The 6-hourly ERA-Interim dataset (Dee et al. 2011) was used for both the analysis and in constructing initial conditions for the ensemble reforecast experiments. The horizontal grid interval is 1.25° longitude by 1.25° latitude with 37 vertical pressure levels extending up to 1 hPa. To conduct the analysis, we first derived daily means from four 6-hourly values for each day.

### b. Experimental setup of ensemble forecast

As in Noguchi et al. (2016), ensemble forecast experiments were conducted using the Meteorological Research Institute Ensemble Prediction System (MRI-EPS) (Yabu et al. 2014). An AGCM used in MRI-EPS is MRI-AGCM, which was developed based on the NWP model of the Japan Meteorological Agency (JMA) (Mizuta et al. 2006, 2012).

The MRI-AGCM has a horizontal resolution of TL159, corresponding to a horizontal grid interval of about 110 km, and has 60 vertical levels of which four levels are above 1 hPa with the top boundary at 0.1 hPa. For dynamical dissipative processes in the stratosphere, the MRI-AGCM implements an orographic gravity wave drag (Palmer et al. 1986; Iwasaki et al. 1989), Rayleigh friction above 50 hPa, and fourth-order horizontal diffusion (JMA 2013). The damping time scale of the horizontal wind due to the gravity wave drag and the Rayleigh friction is estimated to be about 10 and 3 days at 1 and 0.1 hPa, respectively (K. Yoshida, MRI, 2016, personal communication). The ozone concentration was given by the zonal-mean climatology, while the sea surface temperature (SST) was specified by the monthly mean climatology added to a fixed observed anomaly at the initial time of forecasts (see also Noguchi et al. 2016).

Initial perturbations necessary for the ensemble forecast were generated by the MRI-EPS using a breeding of growing mode (BGM) method (Toth and Kalnay 1993). Note that generated perturbations in MRI-EPS are approximated as baroclinically unstable modes in the troposphere, and their amplitude was artificially reduced by a factor proportional to pressure at each vertical level above 100 hPa (Yabu et al. 2014). With addition and subtraction of the generated perturbations to the ERA-Interim dataset, we prepared 24 perturbed initial conditions except for the unperturbed condition comprised only of the ERA-Interim. Then, we conducted each ensemble forecast of 25 members starting at 1200 UTC every day from 20 February to 5 March 2007. The forecast period is 60 days. Daily mean prediction data on 2.5° by 2.5° horizontal grids with 38 vertical pressure levels with a top at 0.4 hPa constructed from 6-hourly model outputs were examined.

## 3. Ensemble forecast experiment

### a. Predictability of the event

First, we examine the predictability of the downward-propagation event of stratospheric planetary waves observed in early March 2007 using the conducted ensemble forecast experiments. Figure 1 shows the meridional

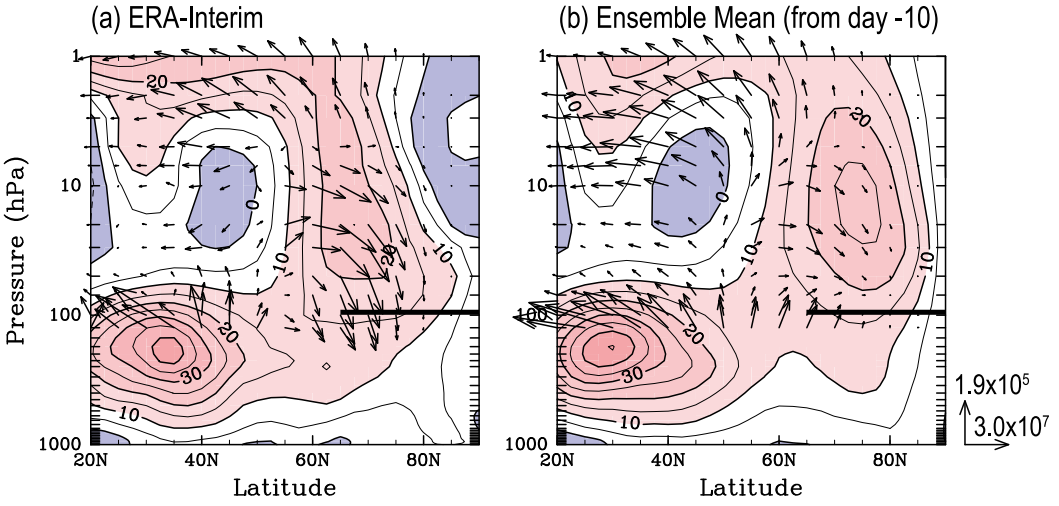


FIG. 1. Meridional distribution of zonal-mean zonal wind (contours; m s$^{-1}$) and E-P flux (arrows; kg s$^{-2}$) on day 0 (5 Mar 2007). (a) The analysis (ERA-Interim). (b) The ensemble-mean prediction starting from day −10 (23 Feb 2007). Contour interval is 5 m s$^{-1}$. Positive (negative) values are indicated by reddish (bluish) colors. E-P flux vectors above 125 hPa are shown and their magnitude is scaled by the inverse of the pressure. Arrows at the right bottom indicate the scale of vertical and meridional components of E-P flux at 1000 hPa. The thick horizontal line at 100 hPa indicates the latitude band used for the definition of EPz100.

profile of zonal-mean zonal wind $\overline{U}$ and Eliassen–Palm (E-P) flux vectors on 5 March 2007 for ERA-Interim (Fig. 1a) and the ensemble-mean forecast (Fig. 1b) starting from 23 February 2007. The observed downward propagation of the wave activity in high latitudes of the stratosphere becomes most prominent on 5 March 2007 (see also Fig. 2), whereas vertical propagation is largely absent for the ensemble-mean prediction. Hereafter, the vertical component of the E-P flux averaged poleward of 65°N at 100 hPa, which is defined as EPz100, is adopted as a measure of the downward propagation of planetary waves in the stratosphere. It is noteworthy that the observed polar night jet has an almost barotropic structure in the vertical with a weak peak in the wind speed in the lower stratosphere. The predicted $\overline{U}$ roughly reproduces the barotropic structure, except for a rather exaggerated peak around 10 hPa.

The predictability of the downward-propagating event is assessed by the time evolution of the predicted EPz100 (Fig. 2). The predicted ensemble mean (red line) of EPz100 on 5 March, when the observed EPz100 (blue line) attains its largest negative value of this period, becomes negative for forecasts starting after 25 February (Fig. 2d). Hereafter, 5 March 2007 is referred to as day 0. Moreover, ensemble spread of EPz100 on day 0 gradually decreases for forecasts starting from day −7 and day −6 (Figs. 2e and 2f). Hence, the predictable period of the downward-propagating event is roughly estimated as 1 week, which is quite short compared with that of a displacement type SSW event in December 2001 (Mukougawa et al. 2005) but is comparable with that of a vortex-splitting-type SSW event in January 2009 (Noguchi et al. 2016).

### b. *Regression analysis*

To reveal a precursory signal for the downward-propagating event in March 2007, we conducted regression analyses with respect to the predicted EPz100 on day 0 using all (25) ensemble members run from the initial condition of day −10 (23 February 2007). In this analysis, the 25 different ensemble-member fields for different days are regressed against EPz100 on day 0. Figure 2b shows that the number of ensemble members predicting a positive EPz100 on day 0 is almost the same as that predicting a negative EPz100 for this ensemble forecast. Hence, we could obtain unbiased regression by using these ensemble members. Note that the polarity of the obtained regression maps in the following figures is reversed to emphasize the downward propagation with a negative EPz100.

First, we examined regression of the predicted E-P flux and its divergence with respect to EPz100 on day 0. The positively (negatively) composited fields of the ensemble mean and the regression (with the opposite sign) from day −3 to day 0 are shown in the top (middle) row of Fig. 3. Hence, the top (middle) row represents the time evolution of ensemble members that predict downward (upward)-propagating planetary waves in the stratosphere on day 0. On day −3, it is found that both composite fields of E-P flux and its divergence are almost the same, and the E-P flux vectors are directed upward and

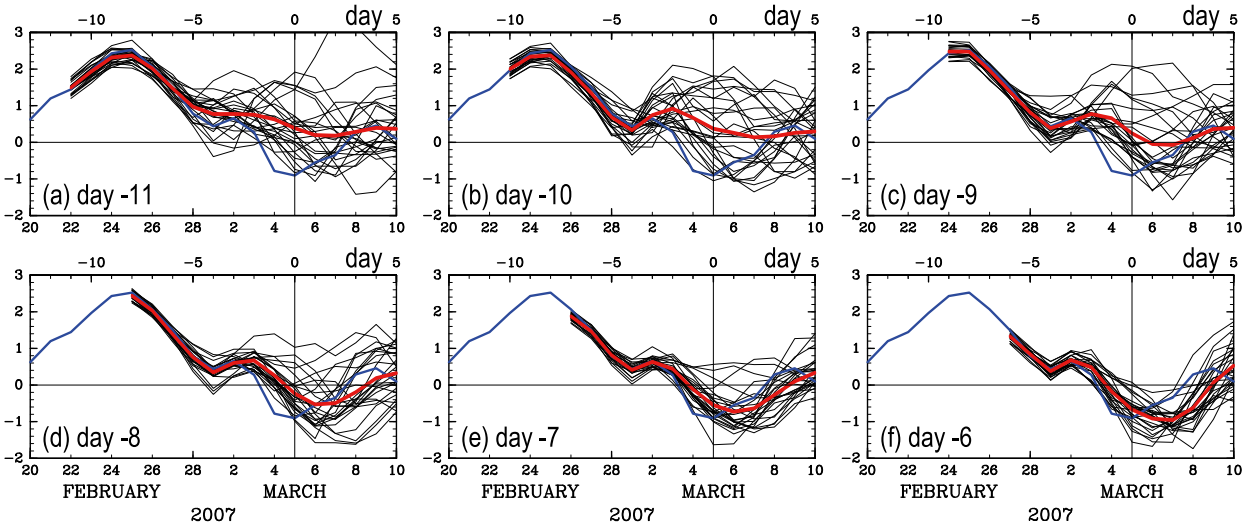


FIG. 2. Time evolution of EPz100 ($10^5$ kg s$^{-2}$). Blue lines indicate the analysis, black lines the prediction of each ensemble member, and red lines the corresponding ensemble mean. The date corresponding to day 0 (5 Mar 2007) is denoted by the vertical line in each panel and the initial date of the forecast is shown in the left-bottom corner of each panel.

equatorward in the stratosphere. Hence, it could be suggested that a strong divergent region of E-P flux in the lower stratosphere poleward of 50°N does not play an important role for the occurrence of the subsequent downward-propagating planetary waves. In fact, the regressed E-P flux divergence in the lower stratosphere has no significant relationship with EPz100 on day 0 as shown in the bottom panel in Fig. 3a. On day −2, we also detect another lower-stratospheric divergent region of E-P flux below 50 hPa around 50°–60°N for both composites (top and middle panels in Fig. 3b), which gradually shifts equatorward and upward. Hence, the downward propagation of stratospheric planetary waves on day 0 has no significant relationship with this lower-stratospheric divergence, too (see bottom panel in Fig. 3b). On the other hand, a region with divergence of E-P flux anomaly that has significant relationship with the downward propagation on day 0 appears on day −2 in the middle and upper stratosphere above 50 hPa around 60°–70°N (bottom panel in Fig. 3b). The downward E-P flux anomaly also emerges there although its magnitude is tiny in the upper stratosphere (bottom panel in Fig. 3b). Then, the significant region gradually extends over the whole stratosphere in high latitudes (bottom panels in Figs. 3c and 3d). We can also detect a large difference in E-P flux divergence field in the middle and upper stratosphere poleward of 60°N between both composites (top and middle panels in Figs. 3c and 3d): in the positive (negative) composite, divergence (convergence) of E-P flux prevails there. Thus, in the following, we will focus on the generating mechanism of the precursory signal detected by the E-P flux diagnosis residing in the stratosphere above 50 hPa before day −2, which is significantly related to the occurrence of the downward propagation of stratospheric planetary waves on day 0.

Regressed anomalies of the zonally asymmetric geopotential height field averaged over 60°–70°N shown in Fig. 4 also support the importance of the precursory signal in the upper stratosphere in exciting the downward-propagating planetary waves. The ensemble-averaged eddy field of the forecast starting from day −10, as shown by contours in Fig. 4, has a westward phase tilt with altitude in the Eastern Hemisphere, corresponding to the upward propagation of the wave packet, as in the observation (Kodera et al. 2008). Then, the wave packet propagates eastward in the upper stratosphere in accordance with the gradual amplification of a ridge around the date line and attenuation of the trough over Europe in the stratosphere. In contradiction to the observation, the quasi-stationary ridge at 180°E has an equivalent barotropic structure with no vertical phase tilt. Hence, the apparent downward propagation of the wave activity is absent for the ensemble-mean prediction on day 0 in the stratosphere, as shown in Fig. 1b. Note that the WN-1 component with maximum amplitude around 5 hPa dominates the ensemble-mean eddy field in the stratosphere. On the other hand, the WN-2 structure prevails over regressed anomalies of eddy components with respect to EPz100 on day 0, especially in the stratosphere of the Western Hemisphere after day −2, as shown by color shading in Fig. 4. A quasi-stationary positive anomaly centered around 240°E and with two negative centers located around 150° and 330°E is conspicuous in the stratosphere. Note that the positive anomaly is located

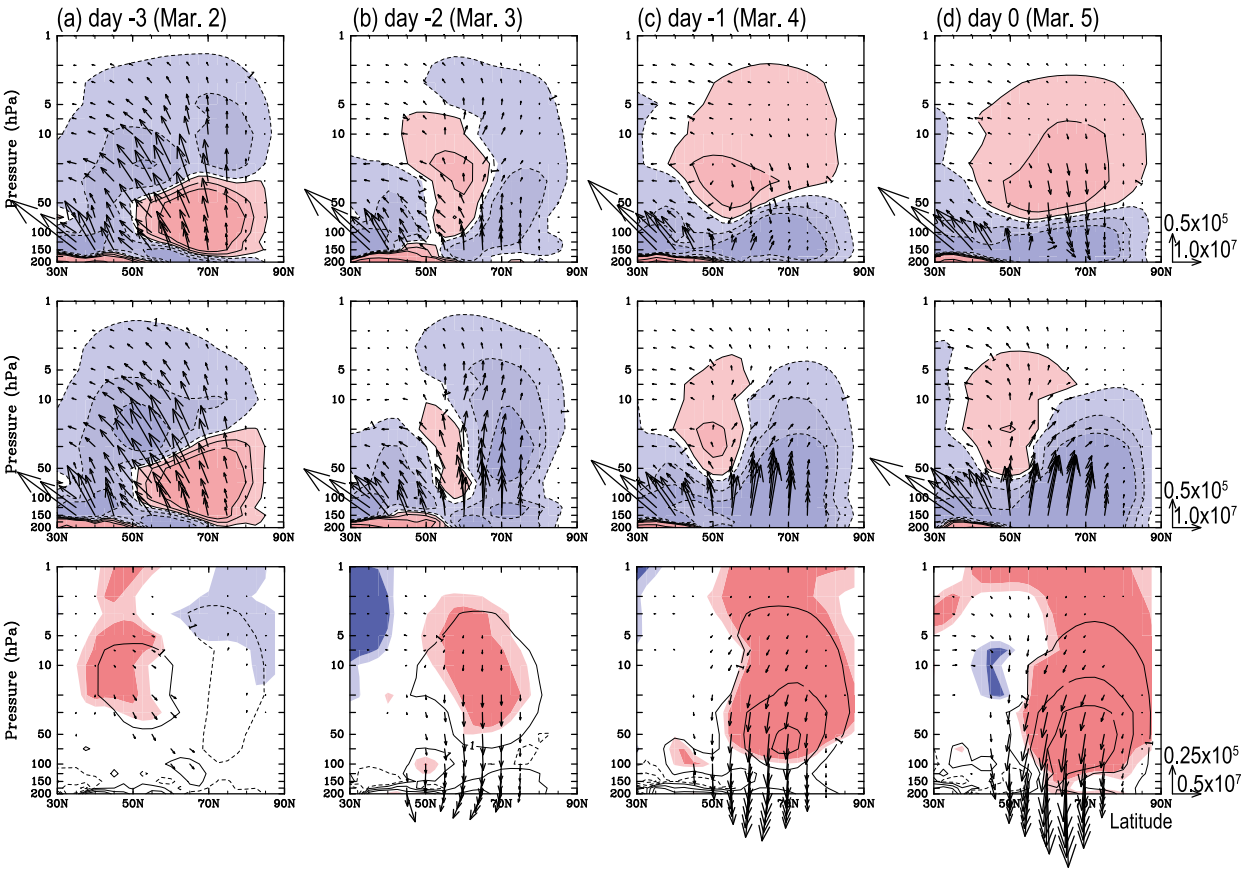


FIG. 3. (top) Composited fields of the ensemble mean and the regression of the predicted E-P flux (arrows; $\mathrm{kg\,s^{-2}}$) and its divergence (contours; $10^{-7}\,\mathrm{kg\,s^{-2}\,m^{-2}}$) from day −3 to day 0 with respect to EPz100 on day 0. (middle) As in (top), but for composited fields of the ensemble mean and the regression of the predicted E-P flux and its divergence with the opposite sign. (bottom) As in (top), but for regressed anomalies of the predicted E-P flux and its divergence. The polarity of the regressed field is reversed. Regressed E-P flux vectors are shown if either the meridional or vertical component of the regressed E-P flux is statistically significant at the 95% level. Regions where the regressed divergence anomaly has a statistical significance at the 95% (99%) level have lighter (darker) shading. Arrows at the right bottom of each row indicate the scale of vertical and meridional components of E-P flux. Contours are drawn at ±1, ±5, ±10, ±50, and, ±100 ($\times 10^{-7}\,\mathrm{kg\,s^{-2}\,m^{-2}}$) for all panels. E-P flux vectors above 150 (200) hPa are shown for (top) and (middle) [(bottom)].

just on the node of the ensemble-averaged eddy field. Moreover, the regressed eddy anomaly has an equivalent barotropic structure in vertical and attains its maximum amplitude in the upper stratosphere as the ensemble-mean eddy field. Before day −3, planetary-scale regressed anomalies with small amplitude are seen in the upper stratosphere, but eddy anomalies with a significant relationship to EPz100 on day 0 are apparently absent in the troposphere. A significant upward component of anomalous E-P flux at the tropopause is also absent during this period (bottom panel of Fig. 3a). Hence, these facts also support our perception that the dynamical origin of the downward-propagating planetary waves resides in the stratosphere.

The vertical-propagating characteristic of stratospheric planetary waves is easily understood by the superposition of the regressed eddy anomaly on the ensemble-mean field owing to their almost 90° out-of-phase relationship. Figure 4 indicates that when the positive (negative) anomaly is located downstream of the stratospheric ridge of the ensemble-mean field, the phase line of the composited field tends to have eastward (westward) tilt with altitude in the Western Hemisphere, and the wave activity tends to propagate downward (upward) in the stratosphere. In fact, the resultant 3D Plumb flux (Plumb 1985) anomaly shown by arrows in Fig. 4, which is defined by the difference between the 3D Plumb flux computed for the composited field and that for the ensemble-mean field, tends to be directed downward in the Western Hemisphere. Hence, the emergence of the barotropic anomaly with dominant WN-2 structure is key for the downward propagation.

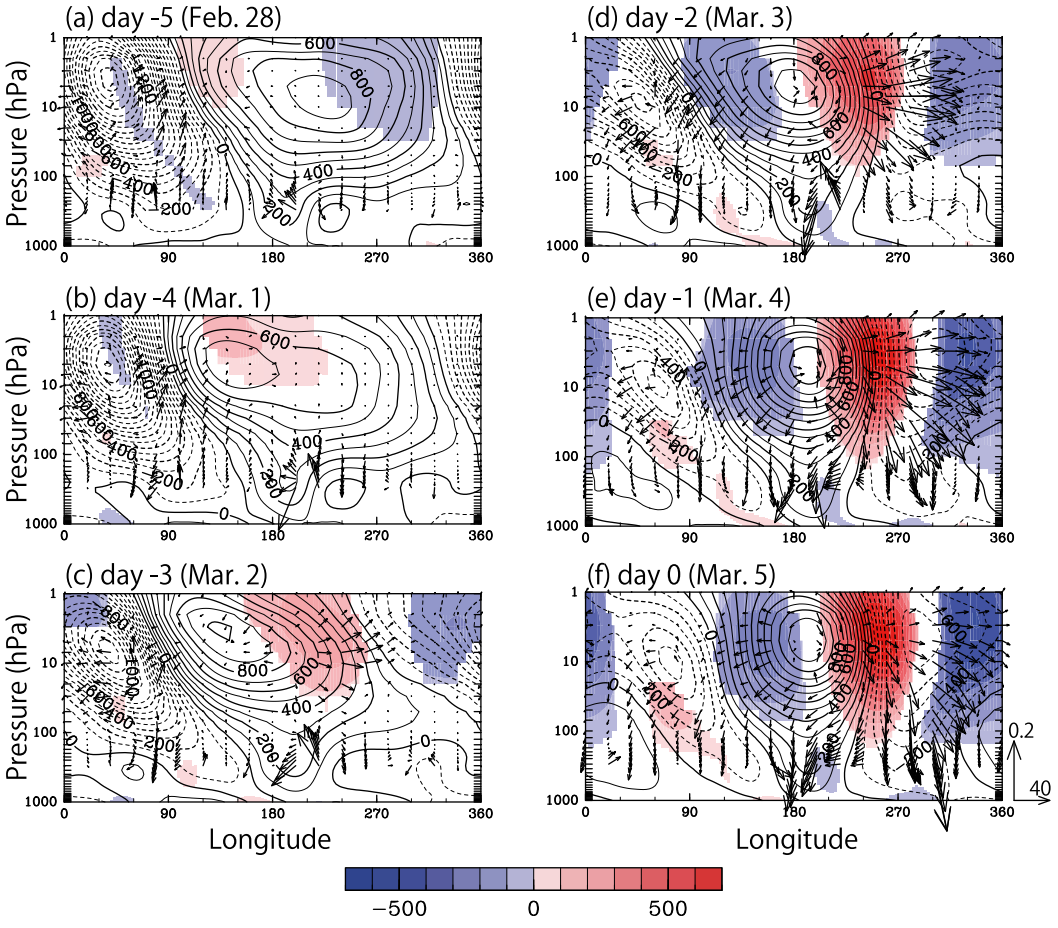


FIG. 4. Longitude–height cross section of the ensemble mean (contours; m) and the regressed anomaly (color shading; m) of the predicted eddy geopotential height averaged over 60°–70°N with respect to EPz100 on day 0. The arrows indicate vertical and zonal components of the anomalous 3D Plumb flux above 300 hPa ($m^2\ s^{-2}$) associated with the composited (ensemble mean plus regressed anomaly) eddy height field. Contour interval is 100 m. Regions where the regressed anomaly has a statistical significance at the 95% level are shaded with different tones designated by the bottom color bar. The 3D Plumb flux is scaled by the inverse of the pressure. Arrows at the right bottom indicate the scale of longitudinal and vertical components of 3D Plumb flux at 1000 hPa.

The polar stereographic map of the 5-hPa geopotential height field shown in Fig. 5 also reveals an amplification of the regressed WN-2 anomaly (color shading) in the upper stratosphere. After day −4 (Fig. 5b), the three anomaly centers along 60°N at 150°, 240°, and 330°E more or less uniformly increase in magnitude with an almost geographically fixed horizontal structure. Moreover, there is no apparent signal of the horizontal energy propagation, in contrast to the ensemble-mean field (contours), which is characterized by an extensively distorted polar vortex. In addition, since the anomaly centers are located at the same high latitudes as the ensemble-mean field, interference between the two fields occurs effectively. Such horizontally uniform amplification of the 5-hPa regressed anomaly with an almost barotropic structure in vertical (Fig. 4) suggests that dynamical instability of the upper-stratospheric circulation, rather than meridionally or vertically propagating waves from elsewhere, is the most likely cause of its amplification.

### c. *Analysis on ensemble spread*

We further examined the time evolution of the ensemble spread in order to explore the relevance of dynamical instability to the growing anomaly. The spread was measured by the root-mean-squared (rms) differences between each ensemble member and the ensemble mean for the predicted 5-hPa geopotential height field northward of 30°N. First, Fig. 6 shows the time evolution of the ensemble spread for each forecast. It

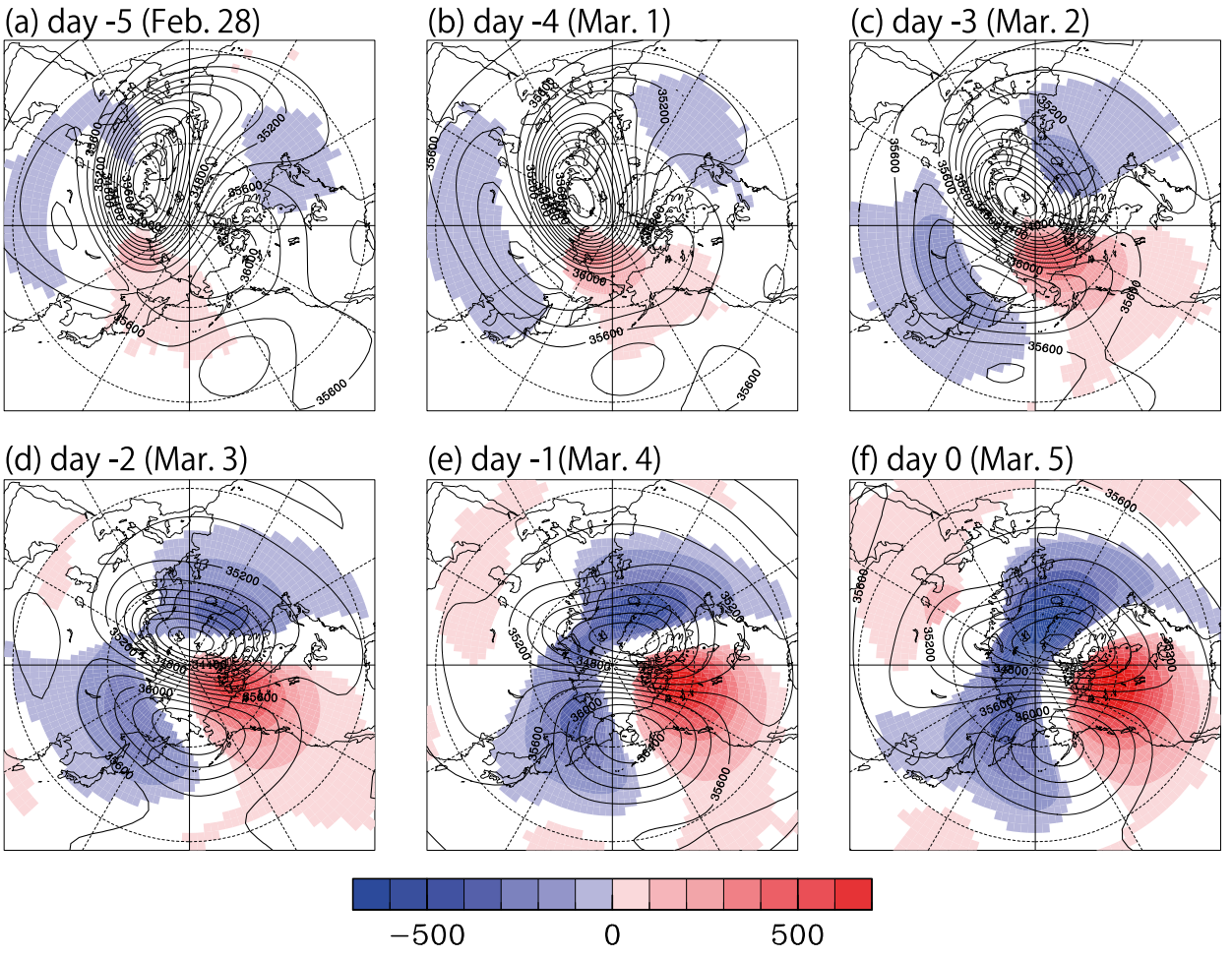


FIG. 5. Horizontal distribution of the ensemble mean (contours; m) and the regressed anomaly (color shading; m) of the predicted 5-hPa geopotential height with respect to EPz100 on day 0. Contour interval is 100 m. Regions where the regressed anomaly has a statistical significance at the 95% level are shaded with different tones designated by the bottom color bar.

is found that spreads for forecasts starting from 21 to 23 February have similar growth rates during the period from 28 February to 3 March; these are larger than those of the other forecasts. This is recognized as the steeper gradient of the spread curves for these forecasts in early March. Moreover, the amplification rate of the spread in the first 24 h of the forecast, which is assessed by the ratio of the spread at the 1-day forecast to the initial spread, attains a maximum of about 2.8 on 28 February, which also implies the quick divergence of nearby trajectories in phase space during this period. Such an enhanced growth of the spread would suggest existence of a "predictability barrier" for the prediction of the upper-stratospheric circulation.

An EOF analysis on difference fields of each ensemble member from the ensemble mean reveals the pattern of greatest spread among members. Figure 7 shows the first EOFs of the difference field for the predicted 5-hPa geopotential height poleward of 30°N during a period from day −5 to day 0 for the ensemble forecast starting from day −10. The resemblance between Figs. 5 and 7 after day −3 is striking in that the first EOFs possess the predominant WN-2 structure as well as the 90° out-of-phase relationship with the ensemble-mean field. The geographical loci of centers of action in the first EOF are also fixed after day −2, which is similar to the quasi stationarity of the regressed anomaly seen in Fig. 5. Moreover, the first EOFs explain about 70% of the total variance of the field among ensemble members during this period. The associated percentage variance explained is indicated by the numeral at the top-right corner of each panel in Fig. 7. Hence, the analyses of the ensemble spread also enforce our supposition that the regressed anomaly shown in Fig. 5 is spontaneously developed as a result of the instability inherent to distorted polar vortex in the upper stratosphere.

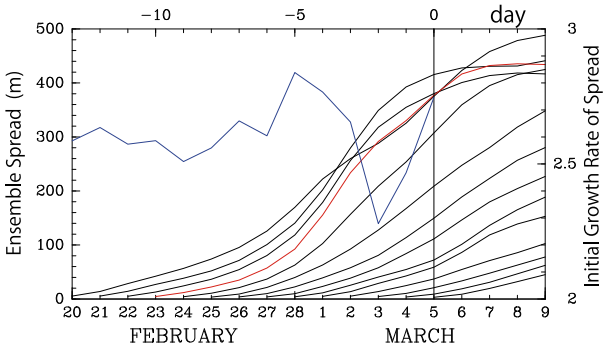


FIG. 6. Time evolution of the rms ensemble spread (m) for the 5-hPa geopotential height field northward of 30°N for each forecast (black lines). The scale is shown by the left ordinate. The abscissa denotes the initial date of each forecast. The red line corresponds to the forecast starting from day −10. The blue line indicates initial growth rate of spread plotted on the initial date of each forecast, which is assessed by the ratio of the spread of the 1-day forecast to the initial spread. Its scale is shown by the right ordinate.

## 4. Stability analysis using a barotropic model

### *a. Model and methodology*

We conduct eigenvalue analysis based on the following nondivergent barotropic vorticity equation on a sphere (cf. Holton and Hakim 2012) to investigate the relevance of the dynamical instability to the source of the obtained regressed anomaly in the upper stratosphere:

$$\frac{\partial \zeta}{\partial t} + J(\psi, \zeta) + \frac{2\Omega}{a^2}\frac{\partial \psi}{\partial \lambda} = F, \tag{1}$$

where $\psi(\lambda, \mu, t)$ is the streamfunction, $\lambda$ the longitude, $\mu$ the sine of the latitude, $t$ the time, $\zeta \equiv \Delta\psi$ the relative vorticity, $\Omega$ the angular velocity of the rotation of Earth with the radius $a$, and the horizontal Laplacian $\Delta$, defined as

$$\Delta \equiv \frac{1}{a^2}\left\{\frac{1}{1-\mu^2}\frac{\partial^2}{\partial \lambda^2} + \frac{\partial}{\partial \mu}\left[(1-\mu^2)\frac{\partial}{\partial \mu}\right]\right\}. \tag{2}$$

The Jacobian $J(\alpha, \beta)$ in Eq. (1) is defined as

$$J(\alpha, \beta) \equiv \frac{1}{a^2}\left(\frac{\partial \alpha}{\partial \lambda}\frac{\partial \beta}{\partial \mu} - \frac{\partial \beta}{\partial \lambda}\frac{\partial \alpha}{\partial \mu}\right), \tag{3}$$

and $F$ on the right-hand side of Eq. (1) indicates the external forcing function representing the vorticity source, for example, due to incoming wave activity flux from the troposphere and several dissipative processes (Hirota 1967). Similar barotropic models have been used to examine the dynamical stability of stratospheric flows (Matsuno and Hirota 1966; Hirota 1967; Manney et al. 1991) and the time evolution of the distorted polar vortex during SSW events (Juckes and McIntyre 1987; Yoden and Ishioka 1993). The almost-barotropic structure of the obtained regressed anomaly and the ensemble-mean field (Fig. 4) as well as the zonal-mean flows in the upper stratosphere (Fig. 1) would also justify the usage of Eq. (1) for our purpose.

Next, to explore the dynamical properties around the basic trajectory representing the evolution of the system in phase space, we divide the flow into two components: a basic flow denoted by an overbar and perturbations denoted by a prime. The basic-flow field with zonally asymmetric components will be given by the ensemble mean in the following analysis; it also satisfies Eq. (1):

$$\frac{\partial \overline{\zeta}}{\partial t} + J(\overline{\psi}, \overline{\zeta}) + \frac{2\Omega}{a^2}\frac{\partial \overline{\psi}}{\partial \lambda} = \overline{F}. \tag{4}$$

When perturbations are assumed to be free from external forcing—that is, $F = \overline{F}$ (Hirota 1967)—we obtain the perturbation equation of motion as

$$\frac{\partial \zeta'}{\partial t} + J(\overline{\psi}, \zeta') + J(\psi', \overline{\zeta}) + J(\psi', \zeta') + \frac{2\Omega}{a^2}\frac{\partial \psi'}{\partial \lambda} = 0 \tag{5}$$

by subtraction of Eq. (4) from Eq. (1). Furthermore, if we assume infinitesimal perturbation, Eq. (5) becomes

$$\frac{\partial \zeta'}{\partial t} + J(\overline{\psi}, \zeta') + J(\psi', \overline{\zeta}) + \frac{2\Omega}{a^2}\frac{\partial \psi'}{\partial \lambda} = \nu\left(\Delta + \frac{2}{a^2}\right)^3 \zeta'. \tag{6}$$

On the right-hand side of Eq. (6), we additionally introduce a scale-selective hyperviscosity term with a coefficient $\nu$ to smooth the numerical behavior (Juckes and McIntyre 1987; Yoden and Ishioka 1993). The second term $+2/a^2$ on the right-hand side is also added to conserve total angular momentum (Ishioka et al. 1999).

The perturbation field is assumed to have a normal-mode form:

$$\psi'(\lambda, \mu, t) = \mathrm{Re}\{\phi(\lambda, \mu)e^{\sigma t}\}, \tag{7}$$

where $\mathrm{Re}\{\cdot\}$ denotes the real part of the expression within the braces, and the basic-flow field as well as $\phi(\lambda, \mu)$ are expanded in spherical harmonics as

$$\phi(\lambda, \mu) = \sum_{n=1}^{N}\sum_{m=-n}^{n} \phi_n^m P_n^m(\mu) e^{im\lambda}, \tag{8}$$

where $P_n^m(\mu)$ represents the associated Legendre functions, $n$ the total wavenumber, and $m$ the zonal wavenumber. Substitution of the expressions for $\phi$ and $\overline{\psi}$ in Eq. (8) into Eq. (6) results in a matrix eigenvalue problem for the complex frequency $\sigma = \sigma_r + i\sigma_i$. An efficient transform

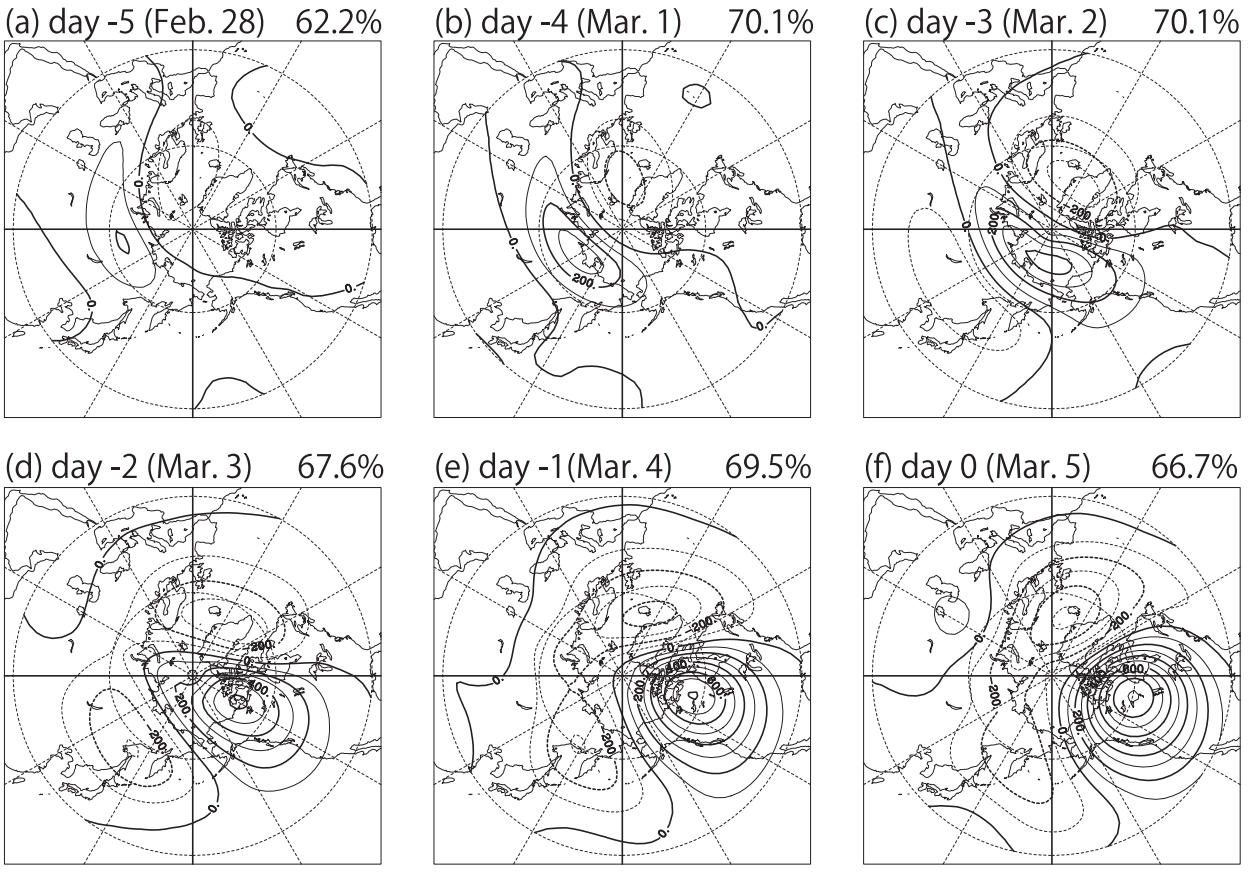


FIG. 7. The first EOFs of the difference field of each ensemble member from the ensemble mean for the predicted 5-hPa geopotential height northward of 30°N (m) on each prediction date of the forecast starting from day −10. Contour interval is 100 m. The corresponding variance explained is shown at the top right of each panel.

code of ISPACK (Ishioka 2016) was employed to conduct the numerical calculations for each term in Eq. (6), and Linear Algebra Package (LAPACK) freeware (Anderson et al. 1999) was used to solve the eigenvalue problem.

### b. *Eigenvalue problem for ensemble-mean field*

The eigenvalues were obtained using a version of the model with a triangular truncation retaining $N = 63$ wavenumbers (T63), of which the spatial resolution is high enough for the convergence of obtained eigenvalues (Anderson 1991). The hyperviscosity coefficient $\nu$ is fixed at a small constant value which gives a dissipation time scale of 0.1 days at the total wavenumber $N = 85$ as in Yoden and Ishioka (1993). The basic streamfunction field was computed from the horizontal wind field of the ensemble-mean prediction. In this computation, the flow field was spatially smoothed to remove smaller-scale flow structures with total wavenumbers larger than $N = 21$. Such smaller-scale structures are especially prominent in the ensemble-mean forecast of a short prediction period.

Figure 8 shows growth rates $\sigma_r$ for obtained unstable modes with values larger than 0.1 day$^{-1}$ for the basic state given by the predicted 5-hPa flow field on each prediction date of the ensemble-mean forecast starting from day −10. Stationary modes with $\sigma_i = 0$ are denoted by red open circles, and transient modes with $\sigma_i \neq 0$ are denoted by black open circles. The growth rate of the most unstable mode attains its maximum at the beginning of March, for which the *e*-folding time is about 1.3 days. It is found that the timing of the attainment of the maximum growth rate is just before the emergence of the characteristic WN-2 regressed anomaly (Figs. 4 and 5), which is roughly concurrent with the rapid increase of the spread (Fig. 6). Moreover, the amplification rate of the spread of the 5-hPa height field during the 24-h forecast, which is about 2.8 and corresponds to a growth rate of ln(2.8) = 1.03 day$^{-1}$, is almost comparable to that of the obtained unstable modes. Hence, the predictability barrier for the prediction of the upper-stratospheric circulation suggested by the time evolution of the spread growth is also represented as the upsurge

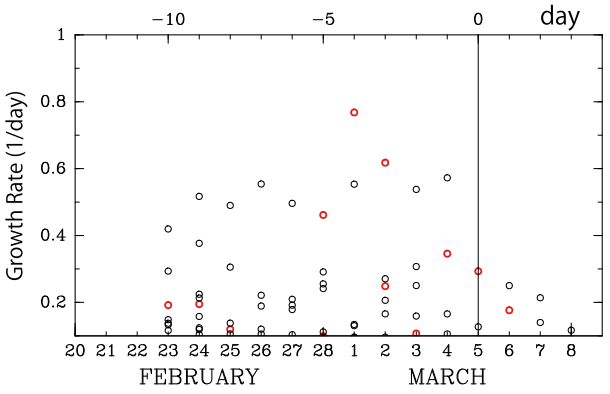


FIG. 8. Growth rate of unstable modes computed for the basic flow composed of the T21 truncated 5-hPa streamfunction of the ensemble-mean field on each prediction date of the forecast starting from day −10 ($day^{-1}$). Red (black) circles correspond to stationary (transient) modes with a zero (nonzero) imaginary component of the eigenvalue.

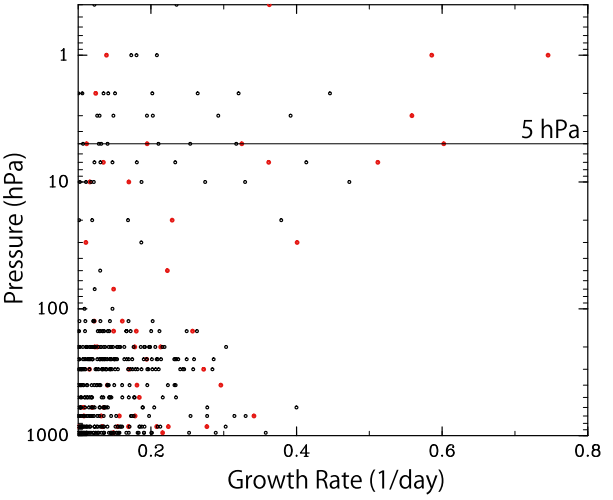


FIG. 9. As in Fig. 8, but for the basic flow composed of the T21 truncated streamfunction field on day −3 at each pressure level for the ensemble-mean prediction starting from day −10.

of the dynamical instability inherent to the upper-stratospheric distorted polar vortex during this period.

The fact that the spread has a somewhat larger growth rate than the fastest-growing mode can be understood by taking account of the contribution of the optimal excitation mechanism to the spread growth during a finite time interval (Mukougawa and Ikeda 1994; Hartmann et al. 1996). It is also interesting to note that the unstable modes obtained for ensemble-mean fields during this analysis period have much larger growth rates than those reported in previous literature, such as Frederiksen (1982) for the basic state of three-dimensional distorted stratospheric polar vortices in the Northern Hemisphere and Manney et al. (1991) for the Southern Hemisphere. Moreover, their growth rates are even larger than those of baroclinically unstable modes in the troposphere (Hirota 1968; Frederiksen 1983). It should be also noted that stationary modes prevail over transient modes during the maximum period of growth rates in early March (Fig. 8).

The very large growth rates of unstable modes for the upper stratosphere can also be seen in Fig. 9, which shows growth rates of unstable modes at each pressure level of the predicted ensemble-mean flow on day −3 of the forecast starting from day −10. Growth rates of unstable modes for the upper-stratospheric flow are more than twice those for the tropospheric and lower-stratospheric flows. In addition, the corresponding *e*-folding times of unstable modes in the upper stratosphere are much shorter than the time scale of the dissipative processes incorporated in MRI-AGCM (see section 2b). Hence, these unstable modes play an invaluable role in the time evolution of the forecast spread of the upper-stratospheric flow field.

Horizontal structures of the obtained unstable modes shown in Fig. 10 also support the relevance of these modes to the forecast spread and the regressed anomaly. The top panels show 5-hPa ensemble-mean flows specified as the basic flow $\overline{\psi}$ in Eq. (6), and the middle and bottom panels show the horizontal structure $\mathrm{Re}\{\phi(\lambda, \mu)\}$ in Eq. (7) of the first and second fastest-growing modes on days −9, −5, −4, and −3. On day −9 when the WN-1 structure dominates the basic flow, both unstable modes are characterized by zonally localized, relatively small-scale disturbances with the WN-6 component along the latitude band of 40°–50°N, corresponding to the edge of the two vortices in the basic flow. During the peak period of the growth rate after day −5, unstable modes tend to have a large amplitude in polar regions, which are characterized by dominant planetary-scale disturbances of the WN-1 and WN-2 components. Note that the basic flow during this period is characterized by an extensively distorted polar vortex, in which an anticyclonic vortex intrudes from Eurasia to the North Pacific owing to a circulation induced by a cyclonic vortex over Scandinavia. It is also interesting to note that we see some similarity in horizontal structure between the fastest-growing modes in Fig. 10 and the first EOFs of the difference field in Fig. 7; the first EOFs on day −3 (Fig. 7c) and day −2 (Fig. 7d) resemble the first unstable modes on day −4 (middle panel in Fig. 10c) and day −3 (Fig. 10d). In particular, the spatial correlation between the most unstable mode on day −3 (Fig. 10d) and the regressed 5-hPa streamfunction field on the principal component associated with the first EOFs of the difference field on day −3 evaluated over a region poleward of 40°N is −0.60, a value that is usually considered to be significant. Both patterns are composed of a dominant WN-2 component including a

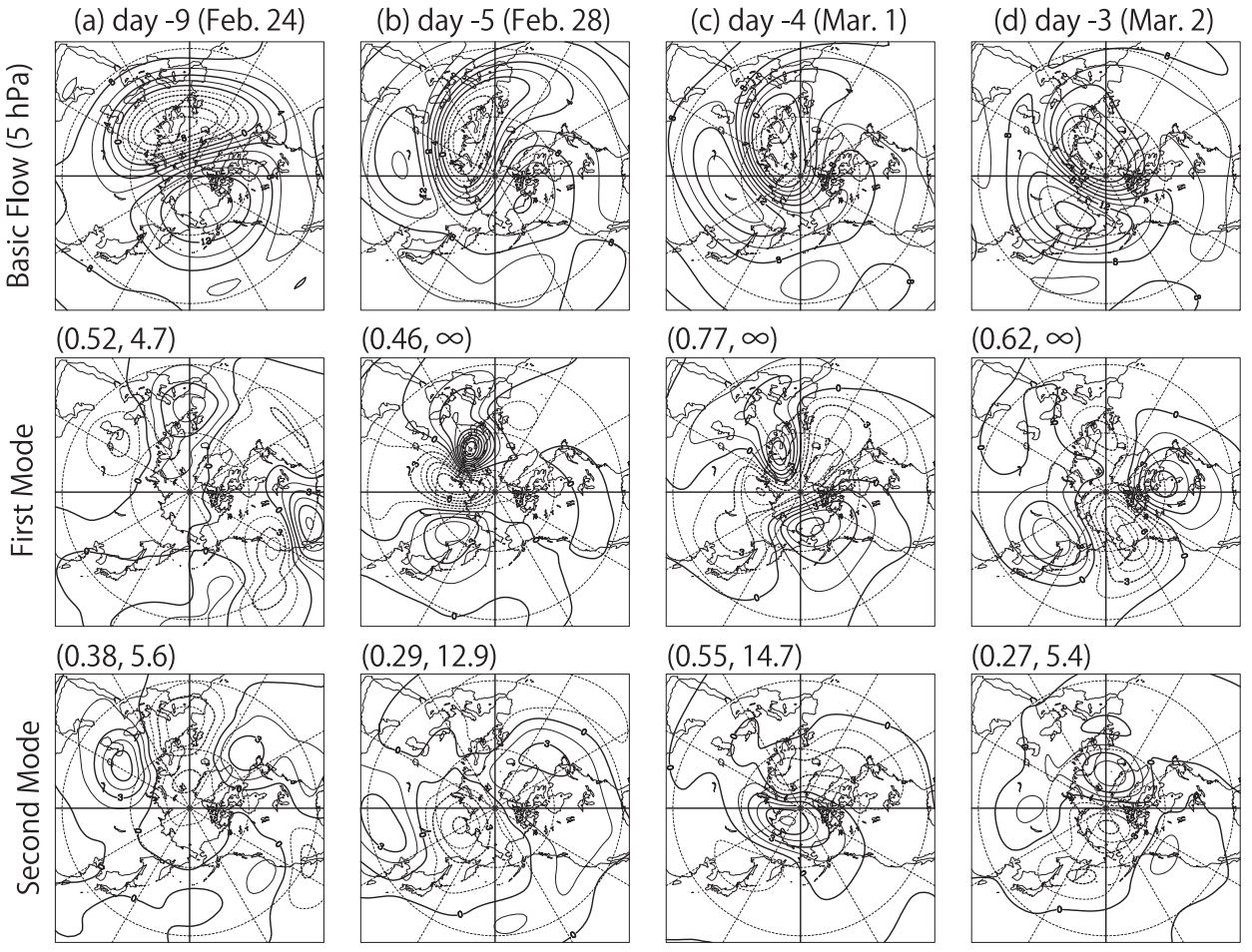


FIG. 10. (top) Horizontal structure of the basic flow given by the T21 truncated 5-hPa streamfunction field ($10^7$ m$^2$ s$^{-1}$) of the ensemble-mean prediction on days (a) −9, (b) −5, (c) −4, and (d) −3 for the forecast starting from day −10. (middle),(bottom) Streamfunction field for the first and second unstable modes computed for the basic flow. The first and second numbers in parentheses above each panel indicate the growth rate (day$^{-1}$) and the period (days) of the unstable mode, respectively. Stationary modes with a zero imaginary component of the eigenvalue are designated by the period of the infinity.

characteristic wave train with centers of action over northeastern Eurasia and Alaska, which are 90° out of phase with the anticyclonic vortex in the ensemble-mean field (Fig. 10d). Hence, these modes tend to shift the upper-stratospheric vortex downstream or upstream depending on their polarity, and they are apt to serve as the precursory disturbance enforcing the downward or upward propagation of incoming planetary waves from the troposphere. The polarity of the unstable mode is determined by the initial perturbation of ensemble forecasts. The predominance of stationary modes with large growth rates from day −5 to day −3 is also helpful in explaining the almost geographically fixed growing property of the first EOF of the difference field after day −3, as seen in Fig. 7.

Thus, the characteristics of the obtained unstable modes for the 5-hPa streamfunction field of the ensemble-mean forecast, characterized by a highly distorted polar vortex, strongly support our hypothesis that the barotropic instability inherent to the upper-stratospheric flow plays a significant role in producing the precursory disturbance that promotes the subsequent downward-propagating planetary waves.

## 5. Summary and discussion

To reveal the predictability of a downward-propagating event of planetary waves in the stratosphere that was observed in early March 2007, we conducted a series of ensemble forecasts starting every day using the MRI-AGCM. It was found that the predictable period of the downward-propagation event is about 7 days. Regression analysis using all members of an ensemble forecast starting 10 days before the occurrence of the downward propagation revealed that amplifying quasi-stationary

planetary-scale anomalies with a predominant WN-2 barotropic structure in polar regions of the upper stratosphere are significantly related to the subsequent downward-propagating event. Moreover, the upper-stratospheric anomalies are 90° out of phase with the ensemble-mean field. On the other hand, there is no significant precursory signal in the troposphere. Thus, the regressed upper-stratospheric anomalies decisively determine whether planetary waves incoming from the troposphere eventually propagate upward or downward by changing their vertical structure, which depends on the polarity of the regression. Namely, when a positive height anomaly of the regressed field lies to the east (west) of the anticyclonic vortex in the ensemble-mean field, planetary-scale stratospheric disturbances in the composited field of the regressed anomaly and ensemble-mean have an eastward (westward) phase tilt with altitude and propagate downward (upward).

Furthermore, an EOF analysis on difference fields of each ensemble member from the ensemble mean of the predicted 5-hPa geopotential height indicated that the growing quasi-stationary planetary-scale disturbances seen in the regressed anomaly have a similar horizontal structure to the pattern of greatest spread among nearby trajectories representing the time evolution of the upper-stratospheric circulation in phase space around the ensemble-mean forecast. In addition, the growth rate of the ensemble spread in the upper stratosphere reaches a maximum prior to the occurrence of the downward-propagation event. The upsurge of the spread growth during this period also suggests the existence of a predictability barrier for the prediction of the upper-stratospheric flow. Hence, we hypothesized that the amplifying barotropic precursory disturbance with quasi-stationary properties emerges as a result of the barotropic instability inherent to the upper-stratospheric circulation.

In fact, the eigenvalue analysis for basic states constituting the zonally varying 5-hPa streamfunction field of the ensemble-mean forecast using a nondivergent barotropic vorticity equation on a sphere supports our hypothesis—that is, the obtained most unstable mode attains a local maximum in growth rate with an *e*-folding time of about 1.3 days and becomes stationary prior to the downward-propagation event. In addition, the growth rate is almost comparable to the amplification rate of the spread during the initial forecast period. Hence, the predictability barrier is understood to be the upsurge of the dynamical instability of the distorted polar vortex. Moreover, the fastest-growing unstable stationary modes with large growth rates prior to the downward-propagation event have predominant WN-1 and WN-2 components in polar regions, the structure of which has a resemblance to the regressed upper-stratospheric anomaly fields in that they satisfy the 90° out-of-phase relationship with the ensemble-mean field. Thus, in early March 2007, the barotropic instability inherent to the distorted polar vortex in the upper stratosphere, which is forced by incoming planetary waves from the troposphere, determines whether the planetary waves are eventually absorbed or emitted downward in the stratosphere.

The extremely large growth rate of the obtained barotropically unstable mode is due to the distorted polar vortex in the upper stratosphere. Figure 11 shows the horizontal structures of unstable modes with the two largest growth rates for the basic flow composed of 5-hPa *zonally symmetric* components (Fig. 11a) of the T21 truncated ensemble-mean prediction field on day −3. Each mode is respectively composed of transient WN-2 and WN-3 components and is centered around 50°–60°N, corresponding to a region with a negative absolute vorticity gradient (Fig. 11a). Hence, these are conventional barotropic unstable modes for zonal flows (Ishioka and Yoden 1992). The growth rates of these modes (0.07 and 0.03 $day^{-1}$) are less than one-tenth those of the unstable modes for the zonally varying basic flow (Fig. 8) and even smaller than the damping time scale of at most several days for the imposed Rayleigh friction in the MRI-AGCM (cf. section 2). Thus, the conventional barotropic instability of stratospheric zonal winds is totally irrelevant to the dynamics, as already noted by Hirota (1967). However, the zonally varying component of the polar vortex is essential to the vigorous barotropic instability of the upper-stratospheric flow during this period.

Next, we argue the relevance of the predicted zonally varying ensemble-mean field to the basic state in the stability analysis. The conventional instability theory has been utilized to reveal the origin of observed fluctuations in the circulations of the real atmosphere. Hence, the eigenvalue analyses have been conducted for the basic flows without fluctuations (Pedlosky 1987), including a highly idealized zonal flow (e.g., Charney 1947; Eady 1949). Although adequately time-averaged zonally varying flows such as climatological flows have been also adopted as the basic state (e.g., Simmons et al. 1983; Anderson 1991), we should realize that the observed fluctuations cannot be attributed to an instability process of such time-averaged states because those states are inevitably affected by the presence of the targeted unstable fluctuations if they exist (Pedlosky 1987). However, the relevance of the ensemble-mean field to the basic state is not of concern in this study. This is because we utilize an instability theory to explain not the dynamical origin for observed fluctuations, but that for the direction of most spreading among the ensemble members. In this framework, the ensemble-mean field is

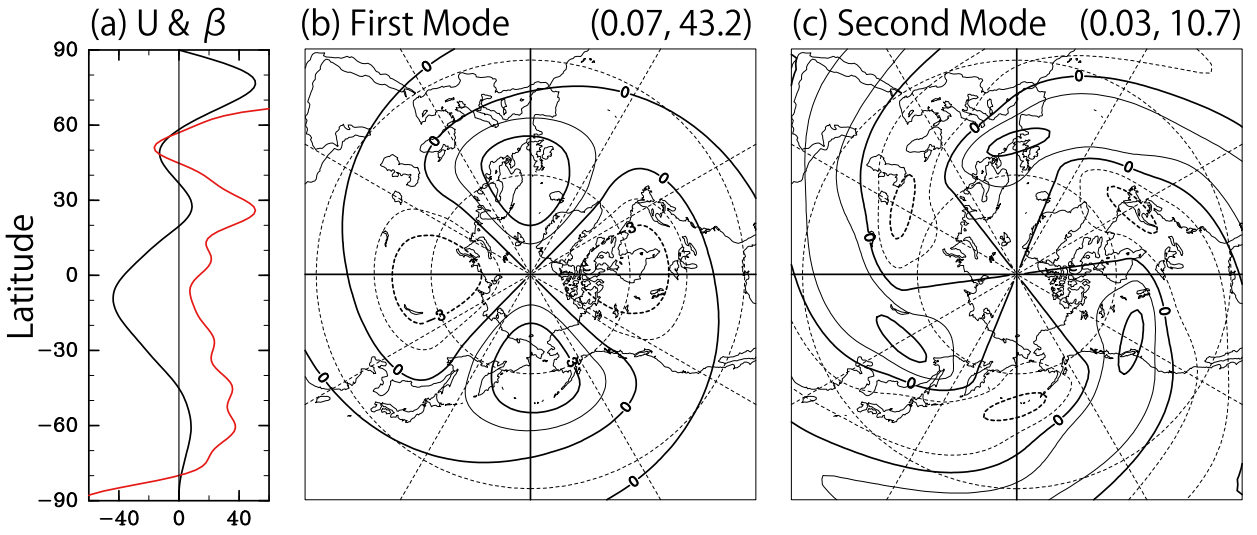


FIG. 11. (a) Meridional profile of the 5-hPa zonal-mean zonal wind (black line; $m\,s^{-1}$) and the corresponding meridional gradient of absolute vorticity (red line; $10^{-11}\,m^{-1}\,s^{-1}$) on day −3 for the ensemble-mean forecast starting from day −10. Horizontal structure for (b) the first and (c) the second unstable modes of the zonally symmetric basic state are also shown. The first and second numbers in parentheses at the top right of (b) and (c) indicate the growth rate ($day^{-1}$) and the period (days) of the unstable mode, respectively.

the most natural choice for the basic state with which to conduct the stability analysis. We have indeed succeeded in understanding the presence of the predictability barrier and the origin of the regressed anomaly in the upper stratosphere within the framework of the barotropic instability of the ensemble-mean field representing the distorted vortex.

It is also tempting to conduct a similar stability analysis by specifying time-averaged observed flows as the basic state to explain the dynamics of the upper-stratospheric flow prior to the downward-propagation event. This is because we could predict the forecast skill of the upper-stratospheric circulation without conducting any ensemble forecasts if the time-averaged observed flows have a similar stability property to the ensemble-mean field. Figure 12 shows the growth rate of the fastest-growing modes for the 3-day running-mean observed 5-hPa streamfunction field with the T21 truncation. The time averaging was conducted to diminish transient disturbances with high frequency. We detect a local maximum of the growth rate during a period from day −7 to day −5. However, the peak is attained 3 days earlier and with a magnitude slightly smaller than that in Fig. 8 for the ensemble-mean field. Hence, the predictability barrier is qualitatively detectable as the upsurge of the dynamical instability of the observed polar vortex.

Unstable modes for the observed flows shown in Fig. 13 also have some horizontal structures similar to those for the ensemble-mean field (Fig. 10). On day −9, the two fastest-growing modes (Fig. 13a) are also characterized by zonally localized wave disturbances along the vortex edge similar to those in Fig. 10a because both basic flows are almost identical owing to a short forecast period of 1 day. During a period from day −5 to day −3, the fastest-growing modes become stationary or quasi stationary and their maximum amplitude occurs in polar regions as shown in Fig. 13; this is in contrast to those on day −9. These properties of unstable modes for the observed flows are also qualitatively similar to those for the ensemble-mean field. However, the detailed wave structure and phase relationship with basic flow are not identical in both kinds of unstable modes, indicating the sensitivity of unstable modes to the basic flow. Thus, the precognition of the predictability barrier by the stability analysis for the observed flows is promising but remains qualitative.

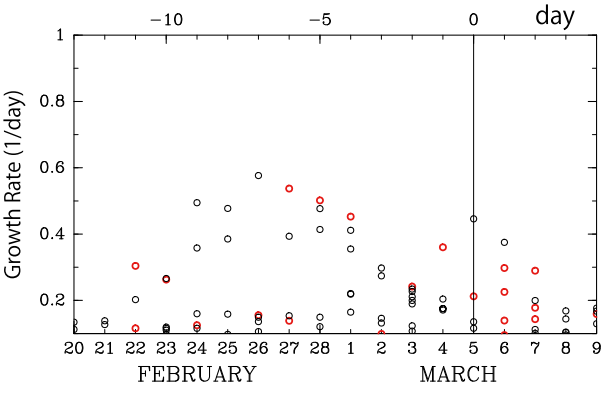


FIG. 12. As in Fig. 8, but for the basic flow composed of the T21 truncated 3-day running-average 5-hPa streamfunction field of the ERA-Interim data.

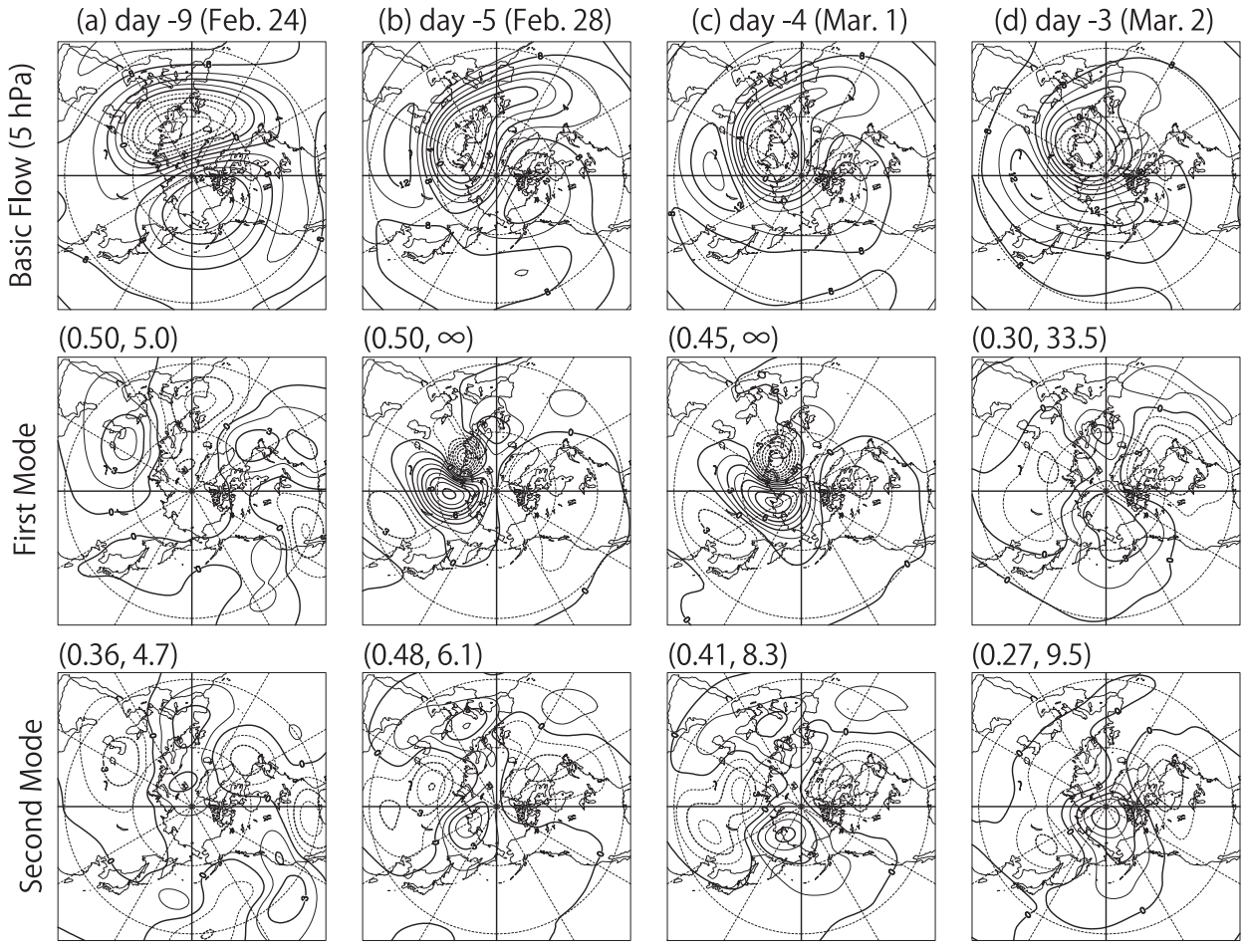


FIG. 13. As in Fig. 10, but for the basic flow given by the 5-hPa streamfunction field of the ERA-Interim data.

The above argument on the basic state should be taken into account when evaluating the pioneering work of Kimoto et al. (1992) in predicting forecast skill during a tropospheric blocking event by computing the error growth rate based on a tangent linear barotropic equation about the observed tropospheric flows. The limited correspondence of the computed error growth rate to the spread of the operational prediction reported in their study would be eased by adopting the ensemble-mean field as the basic state when computing the error growth rate. A more important factor for limiting such correspondence results from the fact that besides the existence of a predominant baroclinic instability in the troposphere, the instability property of the troposphere is different from that of the upper stratosphere, as shown in Fig. 9. Figure 9 reveals that a few unstable modes with large growth rates dominate in the upper stratosphere, whereas many unstable modes with comparable growth rates exit in the troposphere. Hence, it is implied that in comparison with the upper-stratospheric trajectory, the tropospheric trajectory is embedded in a much-higher-dimensional phase space. Such low dimensionality of the upper-stratospheric dynamics would make it possible to describe the spread growth by a few fastest-growing modes in this study. It is also interesting to note that the implication of the difference in dimensionality between the troposphere and stratosphere is also in accordance with the relative importance of the stochastic (deterministic) error growth over the deterministic (stochastic) error growth in the troposphere (stratosphere), as revealed by Inatsu et al. (2013, 2015).

The relevance of the obtained unstable modes to the time evolution of the spread would be quantitatively assured by obtaining singular vectors, which are usually examined in predictability studies (e.g., Hartmann et al. 1996). However, we intentionally did not conduct singular vector calculations based on a tangent linear equation along the basic trajectory in this study. Instead, we conducted eigenvalue analysis about the instantaneous basic state. This is because the former analysis includes an

artificial parameter of a time interval to assess the error growth, and the obtained growth rate depends on the assumed initial perturbations. Along with the fact that the singular vectors grow during a finite time interval even in a dynamically stable basic state (Mukougawa and Ikeda 1994), these artificial factors obscure the dynamical property inherent to the basic state and make it difficult to understand the amplifying mechanism of the ensemble spread. It is also noteworthy that in the context of the predictability study, the veracity of the stability analysis for the instantaneous basic flow is always assured regardless of the growth rate of the obtained unstable modes. Moreover, whether or not the basic flow is a stationary solution of the system does not impair the validity of the analysis since we aim to obtain the spreading directions of nearby trajectories around a point in phase space, which is given by the basic flow.

The relevance of the upper-stratospheric circulation anomaly to the lower-stratospheric circulation should also be quantitatively examined in further studies. For this purpose, it is necessary to conduct eigenvalue analysis and examine the evolution of the regressed upper-stratospheric anomaly using a multilayer model extending from the tropopause to the upper stratosphere. If the obtained 3D unstable modes have a barotropic planetary-scale structure with a considerable vertical extent that is similar to the regressed anomaly shown in Figs. 4 and 5, we can readily stretch the credibility of the barotropic instability of the upper-stratospheric circulation for the generation of downward-propagating planetary waves in the stratosphere. Reforecast experiments starting from initial conditions composed of the superposition of the ensemble-mean field and the regressed upper-stratospheric anomaly will describe the nonlinear evolution of the upper-stratospheric anomaly and its quantitative influence on the lower stratosphere and troposphere. A similar approach was used by Mukougawa et al. (2007) to examine the quantitative impact of Atlantic blocking in the troposphere on the warming of the polar stratospheric region associated with the subsequent SSW event.

Finally, stability analyses on distorted polar vortices in the stratosphere prior to the mature phase of SSW events using a nondivergent barotropic vorticity equation will reveal the important role of the dynamical stability of stratospheric circulation in determining the predictable period of SSW events, which considerably varies from several days to 2 weeks depending on the event (Tripathi et al. 2015; Ichimaru et al. 2016). For example, an SSW event with vortex displacement in December 2001 had a prolonged predictability of 2 weeks (Mukougawa et al. 2005), whereas an event with vortex splitting in January 2009 had a short predictable period of 6 days (Noguchi et al. 2016). The analysis of the spread of the conducted ensemble forecast can easily dictate the predictable period of each event but does not give us any dynamical interpretation as to what factor limits the predictability of each event and why the predictable period differs from one event to another. Hence, if the eigenvalue analysis on the stratospheric basic flow comprising predicted ensemble mean or observed field detects the presence of a predictability barrier with an upsurge of growth rates as in Figs. 8 and 12, we can expect that the in situ barotropic instability of the distorted polar vortex limits the predictable period of the SSW, except for the predictability of tropospheric planetary waves providing the wave forcing to set up the SSW. Our preliminary analysis on the barotropic instability of the polar vortex prior to SSW events in 2001 (2009) provides promising results in which such a predictability barrier is absent (present) prior to the former (latter) SSW event. These results will be presented in a separate paper.

*Acknowledgments.* A spectral transformation library ISPACK (http://www.gfd-dennou.org/arch/ispack/) developed by Prof. K. Ishioka was used to solve the eigenvalue problem for the nondivergent barotropic vorticity equation. The authors thank his kind instruction on how to use the ISPACK library. We would like to thank K. Yoshida for kindly providing information on the dissipative process of the MRI-AGCM. Thanks are also extended to three anonymous reviewers for their thoughtful comments. Figures were drawn using GFD-DENNOU Library. This study was partly supported by Grants-in-Aid for Scientific Research 24224011 and 26287115 funded by Japan Society of the Promotion of Science.

## REFERENCES

Anderson, E., and Coauthors, 1999: LAPACK users' guide, third edition. SIAM, accessed 21 October 2016, http://www.netlib.org/lapack/lug/.

Anderson, J. L., 1991: The robustness of barotropic unstable modes in a zonally varying atmosphere. *J. Atmos. Sci.*, **48**, 2393–2410, doi:10.1175/1520-0469(1991)048<2393:TROBUM>2.0.CO;2.

Baldwin, M. P., and T. J. Dunkerton, 1999: Propagation of the Arctic Oscillation from the stratosphere to the troposphere. *J. Geophys. Res.*, **104**, 30 937–30 946, doi:10.1029/1999JD900445.

——, and ——, 2001: Stratospheric harbingers of anomalous weather regimes. *Science*, **294**, 581–584, doi:10.1126/science.1063315.

Charney, J. G., 1947: The dynamics of long waves in a baroclinic westerly current. *J. Meteor.*, **4**, 136–162, doi:10.1175/1520-0469(1947)004<0136:TDOLWI>2.0.CO;2.

Dee, D. P., and Coauthors, 2011: The ERA-Interim reanalysis: Configuration and performance of the data assimilation system. *Quart. J. Roy. Meteor. Soc.*, **137**, 553–597, doi:10.1002/qj.828.

Eady, E. T., 1949: Long waves and cyclone waves. *Tellus*, **1**, 33–52, doi:10.3402/tellusa.v1i3.8507.

Frederiksen, J. S., 1982: Instability of the three-dimensional distorted stratospheric polar vortex at the onset of the sudden warming. *J. Atmos. Sci.*, **39**, 2313–2329, doi:10.1175/1520-0469(1982)039<2313:IOTTDD>2.0.CO;2.

——, 1983: A unified three-dimensional instability theory of the onset of blocking and cyclogenesis. II: Teleconnection patterns. *J. Atmos. Sci.*, **40**, 2593–2609, doi:10.1175/1520-0469(1983)040<2593:AUTDIT>2.0.CO;2.

Hartmann, D. L., T. N. Palmer, and R. Buizza, 1996: Finite-time instabilities of lower-stratospheric flow. *J. Atmos. Sci.*, **53**, 2129–2143, doi:10.1175/1520-0469(1996)053<2129:FTIOLS>2.0.CO;2.

Hirota, I., 1967: Dynamic instability of the stratospheric polar vortex. *J. Meteor. Soc. Japan*, **45**, 409–421, doi:10.2151/jmsj1965.45.5_409.

——, 1968: On the dynamics of long and ultra-long waves in a baroclinic zonal current. *J. Meteor. Soc. Japan*, **46**, 234–249, doi:10.2151/jmsj1965.46.3_234.

Holton, J. R., and G. J. Hakim, 2012: *An Introduction to Dynamic Meteorology*. 5th ed. Academic Press, 552 pp.

Ichimaru, T., S. Noguchi, T. Hirooka, and H. Mukougawa, 2016: Predictability changes of stratospheric circulations in Northern Hemisphere winter. *J. Meteor. Soc. Japan*, **94**, 7–24, doi:10.2151/jmsj.2016-001.

Inatsu, M., N. Nakano, and H. Mukougawa, 2013: Dynamics and practical predictability of extratropical wintertime low-frequency variability in a low-dimensional system. *J. Atmos. Sci.*, **70**, 939–951, doi:10.1175/JAS-D-12-048.1.

——, ——, S. Kusuoka, and H. Mukougawa, 2015: Predictability of wintertime stratospheric circulation examined using a non-stationary fluctuation–dissipation relation. *J. Atmos. Sci.*, **72**, 774–786, doi:10.1175/JAS-D-14-0088.1.

Ishioka, K., 2016: ISPACK: A FORTRAN77 library for scientific computing. Accessed 21 October 2016, http://www.gfd-dennou.org/arch/ispack/index.htm.en.

——, and S. Yoden, 1992: The stability of zonal flows in barotropic fluid on a rotating sphere. Kyoto University Research Institute for Mathematical Sciences Bulletin Paper 782, 113–124, https://repository.kulib.kyoto-u.ac.jp/dspace/bitstream/2433/82528/1/0782-11.pdf.

——, M. Yamada, Y.-Y. Hayashi, and S. Yoden, 1999: Pattern formation from two-dimensional decaying turbulence on a rotating sphere. Nagare Multimedia, accessed 21 October 2016, http://www2.nagare.or.jp/mm/99/ishioka/.

Iwasaki, T., S. Yamada, and K. Tada, 1989: A parameterization scheme of orographic gravity wave drag with two different vertical partitionings. Part I: Impacts on medium-range forecasts. *J. Meteor. Soc. Japan*, **67**, 11–27, doi:10.2151/jmsj1965.67.1_11.

Japan Meteorological Agency, 2013: Outline of the operational numerical weather prediction at the Japan Meteorological Agency. Appendix to WMO Tech. Progress Rep. on Global Data-Processing and Forecasting System (GDPFS) and Numerical Weather Prediction (NWP), 188 pp., http://www.jma.go.jp/jma/jma-eng/jma-center/nwp/outline2013-nwp/index.htm.

Juckes, M. N., and M. E. McIntyre, 1987: A high-resolution one-layer model of breaking planetary waves in the stratosphere. *Nature*, **328**, 590–596, doi:10.1038/328590a0.

Kimoto, M., H. Mukougawa, and S. Yoden, 1992: Medium-range forecast skill variation and blocking transition: A case study. *Mon. Wea. Rev.*, **120**, 1616–1627, doi:10.1175/1520-0493(1992)120<1616:MRFSVA>2.0.CO;2.

Kodera, K., H. Mukougawa, and S. Itoh, 2008: Tropospheric impact of reflected planetary waves from the stratosphere. *Geophys. Res. Lett.*, **35**, L16806, doi:10.1029/2008GL034575.

——, ——, and A. Fujii, 2013: Influence of the vertical and zonal propagation of stratospheric planetary waves on tropospheric blockings. *J. Geophys. Res. Atmos.*, **118**, 8333–8345, doi:10.1002/jgrd.50650.

Lorenz, E. N., 1965: A study of the predictability of a 28-variable atmospheric model. *Tellus*, **17**, 321–333, doi:10.3402/tellusa.v17i3.9076.

Manney, G. L., C. R. Mechoso, L. S. Elson, and J. D. Farrara, 1991: Planetary-scale waves in the Southern Hemisphere winter and early spring stratosphere: Stability analysis. *J. Atmos. Sci.*, **48**, 2509–2523, doi:10.1175/1520-0469(1991)048<2509:PSWITS>2.0.CO;2.

Matsuno, T., and I. Hirota, 1966: On the dynamical stability of polar vortex in wintertime. *J. Meteor. Soc. Japan*, **44**, 122–128, doi:10.2151/jmsj1965.44.2_122.

Mizuta, R., and Coauthors, 2006: 20-km-mesh global climate simulations using JMA-GSM model—Mean climate states. *J. Meteor. Soc. Japan*, **84**, 165–185, doi:10.2151/jmsj.84.165.

——, and Coauthors, 2012: Climate simulations using MRI-AGCM 3.2 with 20-km grid. *J. Meteor. Soc. Japan*, **90A**, 233–258, doi:10.2151/jmsj.2012-A12.

Mukougawa, H., and T. Ikeda, 1994: Optimal excitation of baroclinic waves in the Eady model. *J. Meteor. Soc. Japan*, **72**, 499–513, doi:10.2151/jmsj1965.72.4_499.

——, M. Kimoto, and S. Yoden, 1991: A relationship between local error growth and quasi-stationary states: Case study in the Lorenz system. *J. Atmos. Sci.*, **48**, 1231–1237, doi:10.1175/1520-0469(1991)048<1231:ARBLEG>2.0.CO;2.

——, H. Sakai, and T. Hirooka, 2005: High sensitivity to the initial condition for the prediction of stratospheric sudden warming. *Geophys. Res. Lett.*, **32**, L17806, doi:10.1029/2005GL022909.

——, T. Hirooka, T. Ichimaru, and Y. Kuroda, 2007: Hindcast AGCM experiments on the predictability of stratospheric sudden warming. *Nonlinear Dynamics in Geosciences*, A. A. Tsonis and J. B. Elsner, Eds., 221–233.

Nese, J. M., 1989: Quantifying local predictability in phase space. *Physica D*, **35**, 237–250, doi:10.1016/0167-2789(89)90105-X.

Noguchi, S., H. Mukougawa, Y. Kuroda, R. Mizuta, S. Yabu, and H. Yoshimura, 2016: Predictability of the stratospheric polar vortex breakdown: An ensemble reforecast experiment for the splitting event in January 2009. *J. Geophys. Res. Atmos.*, **121**, 3388–3404, doi:10.1002/2015JD024581.

Palmer, T. N., G. J. Shutts, and R. Swinbank, 1986: Alleviation of a systematic westerly bias in general circulation and numerical weather prediction models through an orographic gravity wave drag parametrization. *Quart. J. Roy. Meteor. Soc.*, **112**, 1001–1039, doi:10.1002/qj.49711247406.

Pedlosky, J., 1987: *Geophysical Fluid Dynamics*. 2nd ed. Springer-Verlag, 710 pp.

Perlwitz, J., and N. Harnik, 2003: Observational evidence of a stratospheric influence on the troposphere by planetary wave reflection. *J. Climate*, **16**, 3011–3026, doi:10.1175/1520-0442(2003)016<3011:OEOASI>2.0.CO;2.

Plumb, R. A., 1985: On the three-dimensional propagation of stationary waves. *J. Atmos. Sci.*, **42**, 217–229, doi:10.1175/1520-0469(1985)042<0217:OTTDPO>2.0.CO;2.

Simmons, A. J., J. M. Wallace, and G. W. Branstator, 1983: Barotropic wave propagation and instability, and atmospheric teleconnection patterns. *J. Atmos. Sci.*, **40**, 1363–1392, doi:10.1175/1520-0469(1983)040<1363:BWPAIA>2.0.CO;2.

Tomikawa, Y., 2010: Persistence of easterly wind during major stratospheric sudden warmings. *J. Climate*, **23**, 5258–5267, doi:10.1175/2010JCLI3507.1.

Toth, Z., and E. Kalnay, 1993: Ensemble forecasting at NMC: The generation of perturbations. *Bull. Amer. Meteor. Soc.*, **74**, 2317–2330, doi:10.1175/1520-0477(1993)074<2317:EFANTG>2.0.CO;2.

Tripathi, O. P., and Coauthors, 2015: The predictability of the extratropical stratosphere on monthly time-scales and its impact on the skill of tropospheric forecasts. *Quart. J. Roy. Meteor. Soc.*, **141**, 987–1003, doi:10.1002/qj.2432.

Yabu, S., R. Mizuta, H. Yoshimura, Y. Kuroda, and H. Mukougawa, 2014: Meteorological Research Institute Ensemble Prediction System (MRI-EPS) for climate research. Meteorological Research Institute Tech. Rep. 71, 63 pp., doi:10.11483/mritechrepo.71.

Yoden, S., and K. Ishioka, 1993: A numerical experiment on the breakdown of a polar vortex due to forced Rossby waves. *J. Meteor. Soc. Japan*, **71**, 59–72, doi:10.2151/jmsj1965.71.1_59.